Different failure modes for V-containing and V-free AB_2 metal hydride alloys

K. Young [a,*], D.F. Wong [a,b], S. Yasuoka [c], J. Ishida [c], J. Nei [a], J. Koch [a]

[a] BASF Battery Materials-Ovonic, 2983 Waterview Drive, Rochester Hills, MI 48309, USA
[b] Department of Chemical Engineering and Materials Science, Wayne State University, MI 48202, USA
[c] FDK Twicell Co., Ltd. 307-2 Koyagimachi, Takasaki 370-0071, Gunma, Japan

HIGHLIGHTS

- The capacity loss in V-containing AB_2 alloy is first slow and then faster.
- The capacity in the V-free AB_2 shows a consistent degradation.
- Failure mode of former is the formation of thick oxide on the surface.
- Failure mode of later is the continuous pulverization of the particles.

ARTICLE INFO

ABSTRACT

Failure modes of a V-containing and a V-free AB_2 Laves phase-based metal hydride alloy were studied by the combination of X-ray diffractometer, scanning electron microscope, X-ray energy dispersive spectroscopy, inductively coupled plasma, Soxhlet extraction, and magnetic susceptibility measurement. Cells with the V-containing alloy exhibited less capacity degradation up until venting occurred in the cells, after which the capacity rapidly degraded. Cells with the V-free alloy remained linear in capacity degradation throughout the cycle life test. The failure mechanism for the V-containing alloy is related to the formation of an oxide layer that penetrates deeper into the alloy particles due to high V leaching and impedes gas recombination, while the failure mechanism for the V-free alloy is related to the continuous pulverization of the main AB_2 phase.

1. Introduction

Nickel/metal hydride (Ni/MH) rechargeable batteries are widely used in consumer portable devices and hybrid electric vehicles, and development for these applications has a heavy emphasis on improving gravimetric energy density. While the conventional misch metal-based AB_5 metal hydride (MH) alloy has a storage capacity of about 330 mAh g^{-1}, AB_2 [1,2] and A_2B_7 [3] MH alloys have capacities as high as 440 and 410 mAh g^{-1}, respectively, and will boost the gravimetric energy density found in Ni/MH batteries. Properties relating to the structure, hydrogen storage, and electrochemistry of these new alloys have been reported extensively (for a review of research activities in these areas, see Ref. [4]); however, not much work has been reported

regarding the failure mode analysis of these new alloys — an essential step of any new material development process. In a recent report, we compared the failure mode of La-only A_2B_7 alloy in a 70% state-of-charge cycling scheme to that of conventional AB_5 [5]. While the La-only A_2B_7 cell suffers from alloy pulverization, the AB_5 cell degrades due to alloy oxidation and consequent poisoning of the positive electrode.

V is an important modifying element used in AB_2 MH alloys to increase the storage capacity [6–11], facilitate activation [8], and improve both high-rate dischargeability [12] and cycle stability [13] in the Ni/MH negative electrode. However, the cost of V is much higher than other elements used in the typical AB_2 MH alloy formula. Studies optimizing composition [14] and modifier selection [15] were performed previously on V-free AB_2 MH alloys to reduce the raw material cost. In this paper, we will compare the failure modes of two Laves phase-based AB_2 MH alloys: one with V and one that is V-free that came out of the studies.

* Corresponding author. Tel.: +1 248 293 7000; fax: +1 248 299 4520.
E-mail addresses: kwoyoung@yahoo.com, kwo.young@basf.com (K. Young).

Table 1
Structure, gaseous phase, electrochemical, and magnetic susceptibility properties comparison of Alloys A and B.

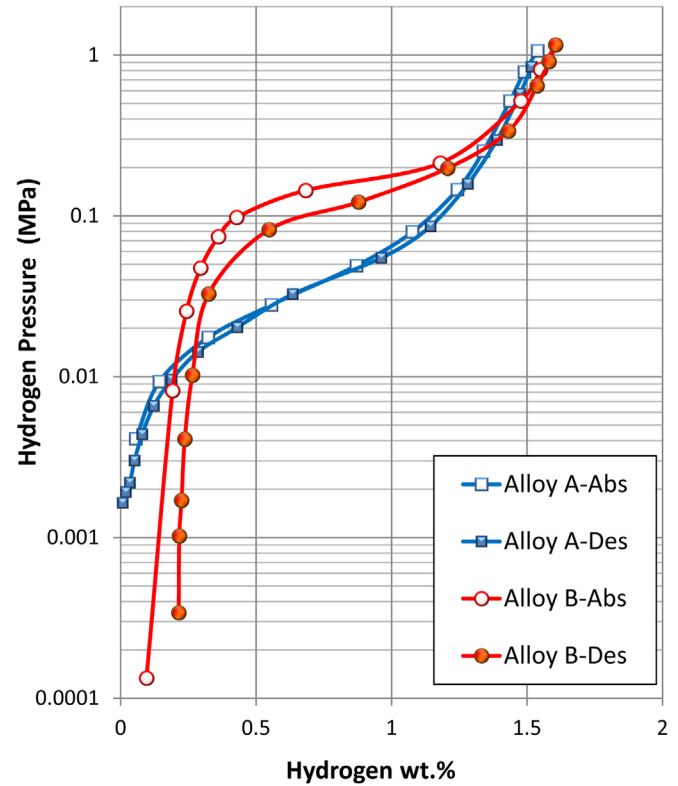|	Composition	Phase abundances	H-storage (wt.%)	Mid-point pressure (MPa)	PCT hysteresis	Cap. @ 50 mA g^{-1} (mAh g^{-1})	Cap. @ 5 mA g^{-1} (mAh g^{-1})	HRD	M_S (memu g^{-1})	$H_{1/2}$ (kOe)
Alloy A	Ti$_{12}$Zr$_{21.5}$V$_{10}$Ni$_{37.7}$Mn$_{13.5}$Cr$_{4.5}$Al$_{0.5}$Sn$_{0.3}$	78% C14, 20% C15, 1% Zr$_7$Ni$_{10}$, 1% Zr$_9$Ni$_{11}$	1.51	0.04	0.02	388	398	0.97	39	0.14
Alloy B	Ti$_{10}$Zr$_{27}$Ni$_{35}$Co$_5$Mn$_{15}$Cr$_8$Al$_{0.1}$	38% C14, 52% C15, 2.3% Zr$_7$Ni$_{10}$, 0.5% Zr$_9$Ni$_{11}$, 7% TiNi	1.61	0.12	0.42	341	374	0.91	27	0.60

Fig. 1. PCT isotherms of Alloys A and B measured at 30 °C. Open and solid symbols are for absorption and desorption curves, respectively. The V-free alloy (Alloy B) shows a higher maximum storage capacity, a lower reversible storage capacity, a higher and flatter plateau, and a higher hysteresis.

2. Experimental setup

Induction melting from elementary raw materials was performed under an argon atmosphere in a 25 kg induction melting furnace using an MgO crucible, an alumina tundish, and a steel cylindrical mold. Ingots were first hydrided/dehydrided and then mechanically crushed into −200 mesh powder. The chemical composition of each sample was examined by a Varian *Liberty* 100 inductively-coupled plasma (ICP) system. A Philips *X'Pert Pro* X-ray diffractometer (XRD) was used to study the microstructure, and a JEOL-*JSM6320F* scanning electron microscope (SEM) with energy dispersive spectroscopy (EDS) capability was used to study the phase distribution and composition. Pressure−concentration−temperature (PCT) characteristics for each sample were measured using a Suzuki-Shokan multi-channel PCT system. Half-cell testing was performed using an Arbin Instruments BT4+ Portable Battery Test System. Magnetic susceptibility was measured using a Digital Measurement Systems Model 880 vibrating sample magnetometer. For full-cell testing, alloy powder was mixed with binder, pasted onto perforated Ni-plated stainless steel plate, dried, and compacted into negative electrodes. AA-sized cylindrical cells were assembled with pasted negative electrode, pasted Ni(OH)$_2$-based positive electrode, polypropylene/polyethylene grafted separator, and 30% KOH electrolyte. The cell design is targeted at a negative-to-positive ratio of 1.4 with a capacity of 1800 mAh. The MH alloy loading is around 7.2 g per cell.

3. Results and discussion

3.1. Alloy properties

The composition, phase distribution, PCT characteristics, electrochemical properties, and magnetic susceptibility properties of

Alloy A (containing 10 at.% V) and Alloy B (V-free) are listed in Table 1. Alloy A was chosen for its good balance between storage capacity and high-rate dischargeability (HRD) among V-containing alloys. Alloy B is a V-free alloy developed from a previous compositional optimization study and exhibits a good balance of several electrochemical characteristics, including capacity, HRD and cycle life [14]. While Alloy B has larger gaseous phase hydrogen storage capacity than Alloy A, the electrochemical capacity is lower for Alloy B. The difference between gaseous phase and electrochemical performances can be explained by the PCT isotherm comparison shown in Fig. 1. A portion of the maximum hydrogen storage capacity in Alloy B can only be realized at very low pressure. In other words, the gaseous phase capacity of Alloy B is not fully reversible within a limited pressure (or voltage) range. This non-reversible portion of the PCT isotherm for Alloy B may be attributed to the 7% TiNi phase (determined by XRD analysis), which has a stronger metal-to-hydrogen bond and slower kinetics. In general, alloys with lower plateau pressures indicate the formation of more stable hydrides, and the stronger metal-to-hydrogen bond strength releases hydrogen at slower desorption rates [16]. However, in this study, Alloy A has a lower hydrogen equilibrium plateau pressure (Fig. 1) but a higher HRD value (Table 1) compared to Alloy B. This discrepancy can be explained by the magnetic susceptibility. The saturated magnetic susceptibility (M_S) is proportional to the total amount of metallic nickel (active catalyst for water splitting and recombination reactions) embedded in the alloy surface oxide after the formation process, and the metallic nickel inclusions are shown to have a direct influence on high-power performance at both room and low temperatures [17]. The higher M_S value for Alloy A correlates to better HRD performance, likely due to the severity of V corrosion in KOH solution generating a higher amount of metallic nickel on the surface. $H_{1/2}$ is the strength of the applied magnetic field necessary to generate magnetic susceptibility equal to half of the M_S value. The applied magnetic field H is inversely proportional to the number of Ni atoms in a cluster by the Langevin function [18]

$$M(H) - \chi_B H = M_S \left\{ \coth\left(\frac{\mu H}{kT}\right) - \frac{kT}{\mu H} \right\} \tag{1}$$

with $H_{1/2}$ defined as

$$\coth\left(\frac{\mu H_{1/2}}{kT}\right) - \frac{kT}{\mu H_{1/2}} = \frac{1}{2} \tag{2}$$

where χ_B is the intrinsic paramagnetic susceptibility of the alloy (estimated by the value of high field magnetization), M_S is the saturation magnetization of ferromagnetic metallic Ni or Ni-alloy nanoparticles, μ is the average magnetic moment of each metallic cluster, k is the Boltzmann constant, and T is the absolute temperature. The $H_{1/2}$ values indicate that the Ni clusters in Alloy A have an average volume 4 times larger than that of Alloy B, but the total number of Ni clusters in Alloy A is only half of that of Alloy B.

3.2. Failure analysis

Two different cycling conditions were applied to the cells used to test the two alloys. Method 1 used a C/2 charge rate with a negative $-\Delta V$ cut-off of 3 mV followed by a discharge at C/2 rate to 0.9 V. Method 2 used a 1C rate for charge and discharge, a discharge cut-off voltage of 0.9 V, and a negative $-\Delta V$ cut-off of 5 mV. The wider $-\Delta V$ cut-off allows for a slightly higher amount of overcharge. Capacities obtained from Cells A1 (Alloy A with Method 1), B1 (Alloy B with Method 1), A2 (Alloy A with Method 2), and B2 (Alloy B with Method 2) are plotted in Fig. 2. Method 1 with lower charge/discharge currents and less overcharge exhibits higher

capacity and longer cycle life compared to Method 2. With both methods, cells with Alloy A show slower capacity degradation in the first 75% of cycle life but loses capacity more rapidly afterward. This results in shorter cycle life in Cells A1 and A2 compared to cells with Alloy B, where linear capacity degradation is observed throughout the entire cycle testing. The difference in capacity degradation behavior suggests that Alloys A and B do not share the same failure mode.

The cycled cells were taken apart in a glove box for further analysis. The positive and negative electrodes from each of the cells were washed in separate Soxhlet extractors and then dried for XRD and SEM/EDS studies. The resulting backscattered electron images (BEI) of the positive electrodes from Cells A1 and B1 are shown in Fig. 3a and b, respectively. At the end of cycle life, positive electrodes from both cells still appear intact. No evidence of pulverization, a source of positive electrode capacity loss, can be found in either electrode. Although the mechanical integrities of the two positive electrodes are the same, the EDS results are different. There are no foreign elements detected in the positive electrode from Cell A1, while foreign Al, Ti, and Mn are detected in the positive electrode from Cell B1. The EDS results of 16 spots identified in Fig. 3b for Cell B1 are summarized in Table 2. The X-ray lines used and the 3
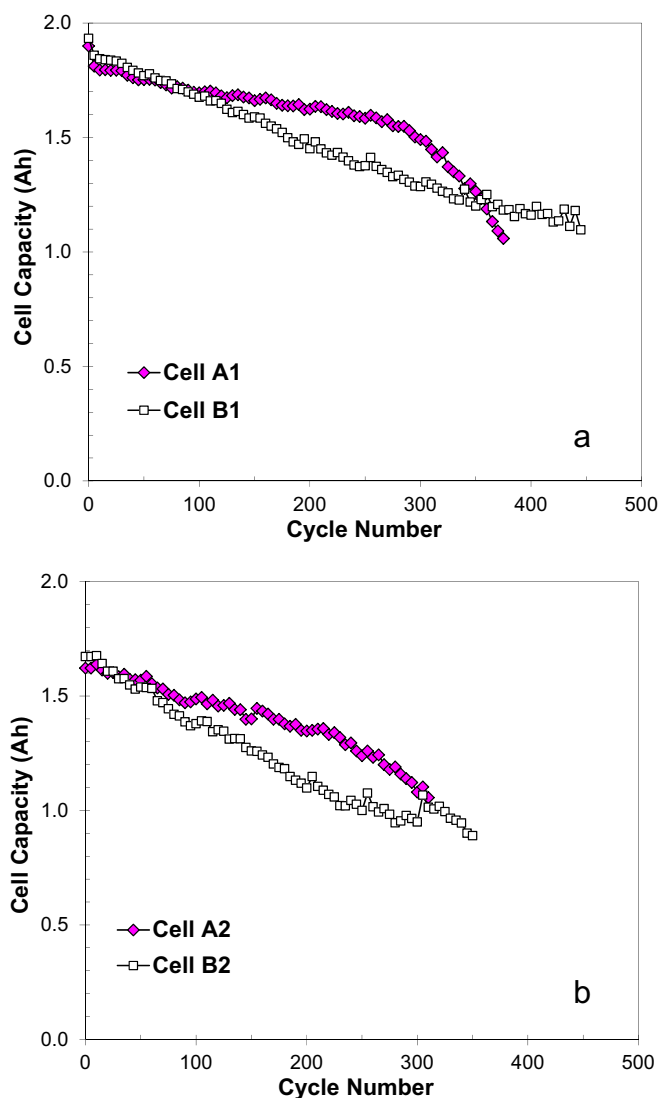

Fig. 2. Plot of discharge capacity vs. cycle number for cells under Method 1 (C/2–C/2) (a) and Method 2 (1C–1C) cycling conditions.
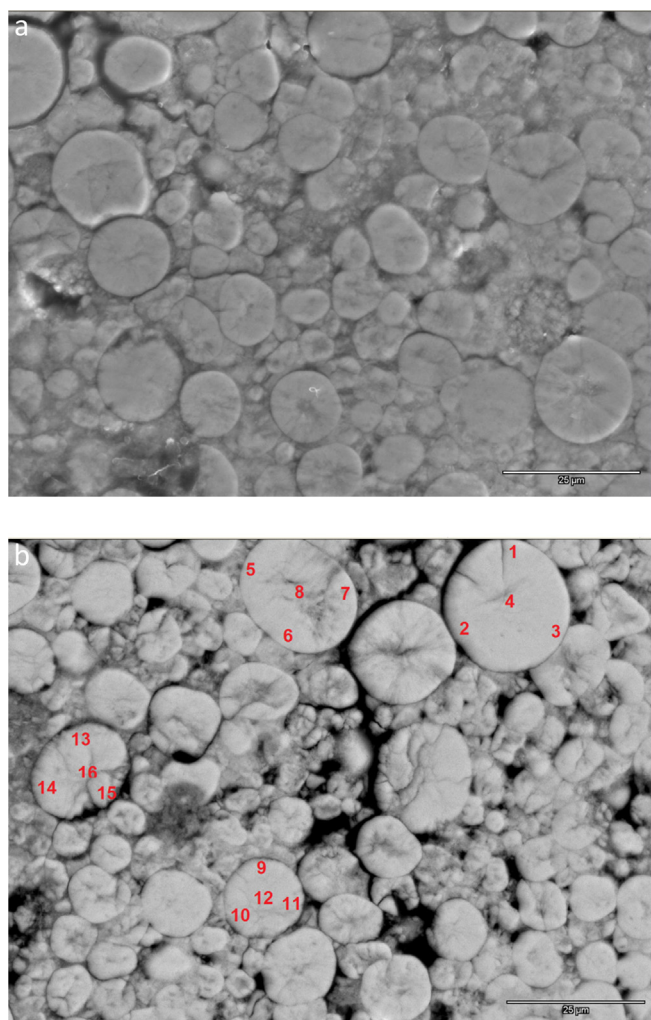
Fig. 3. SEM BEI micrographs of the positive electrodes from Cells A1 (a) and B1 (b).

sigma error bars are also included at the end of the Table. Some of the Al, Mn, Y values are near the detection limit and less reliable than the others. Al is seen in all particles (0.1–0.7 at.%), and the distribution in the particles varies. Ti is also seen in all particles

Table 2
Chemical compositions of several spots identified in the SEM BEI micrograph of the positive electrode from Cell B1 (Fig. 3b). Spots 4, 8, 12, and 16 are from the center while others are from the near-surface of the Ni(OH)$_2$ particles.

EDS location	Al	Ti	Mn	Co	Zn	Y	Ni
1	0.3	0.3	0.1	4.3	6.4	0.1	88.5
2	0.1	0.3	0.0	3.5	6.7	0.0	89.4
3	0.0	0.2	0.0	3.8	6.6	0.0	89.4
4	0.0	0.2	0.0	2.1	6.1	0.0	91.6
5	0.0	0.4	0.0	4.7	6.4	0.0	88.5
6	0.2	0.4	0.0	2.7	6.5	0.0	90.2
7	0.2	0.4	0.0	2.6	6.3	1.0	89.5
8	0.1	0.4	0.0	1.9	6.1	0.0	91.5
9	0.6	0.4	0.1	4.1	6.4	0.0	88.4
10	0.0	0.4	0.1	4.0	6.6	0.0	88.9
11	0.7	0.3	0.0	4.1	6.1	0.0	88.8
12	0.3	0.7	0.2	2.3	5.8	0.0	90.7
13	0.1	0.2	0.0	2.5	6.7	0.0	90.5
14	0.1	0.2	0.0	2.7	6.6	0.0	90.4
15	0.2	0.2	0.0	5.5	6.6	0.0	87.5
16	0.2	0.2	0.1	2.0	6.4	0.0	91.1
Line used	K	K	K	K	K	L	K
Error (±3 sigma)	0.1	0.1	0.1	0.3	0.6	0.2	1.2

(0.2–0.7 at.%), but the distribution in each particle is uniform. Low levels of Mn (0.1–0.2 at.%) can be observed in some particles. Co-content at the surface of the particles is higher than at the center due to the Co-coated Ni(OH)$_2$ powder used in this study. Zn was added during the co-precipitation of Ni(OH)$_2$ to prevent formation of γ-NiOOH during cycling, and its content is consistent throughout the entire positive electrode sample. Although contamination was found in the positive electrode of Cell B1, it does not appear to destroy the conductive Co-network on the surface of the Ni(OH)$_2$ positive electrode. XRD patterns of the positive electrodes from Cells A1 and B1 are shown in Fig. 4a and b, respectively. All peaks can be fit into a β-Ni(OH)$_2$ structure. Al contamination in the positive electrode can promote α-Ni(OH)$_2$ formation in AB$_5$ MH alloy-based cells [19,20], but it does not appear to be the case with the Al leaching observed in Cell B1. The lack of γ-NiOOH characteristic peaks that can form with overcharging also indicates that the Co-conductive network in the positive electrodes remains intact [21]. Both SEM/EDS and XRD analyses suggest that the positive electrode is not the cause of capacity degradation during cycling. Soxhlet extraction experiments were conducted on components from Cells A2 and B2. Soluble contents extracted from the components of each cell were analyzed by ICP, and the results are summarized in Table 3. While the extraction solutions of the positive electrodes from both cells contain comparable levels of Zr, Ti, Al, and Mn, the V-content in the extraction solutions from Cell A2 is very high. Compared to the oxidation products of the other metals, the oxidation product of V is much more soluble in water [22], and it is easily washed into the extraction liquid. Both the EDS and ICP of the positive electrode after extraction show no evidence of V.

SEM results from the negative electrodes of Cells A1 and B1 are presented in Fig. 5. In order to identify the secondary phases and oxides in the alloys, both secondary electron image (SEI) and BEI are shown. While the SEI micrographs only depict surface topography, BEI micrographs also include compositional information in the images: brighter areas of contrast indicate a higher average atomic mass. The main difference between the two alloys in this study is particle integrity. While the particle size and shape of the V-containing alloy in Cell A1 remains about the same at the end of cycle life, the V-free alloy in Cell B1 undergoes severe pulverization. The EDS results of several spots in each BEI micrograph are listed in Table 4. AB$_2$ and Zr$_7$Ni$_{10}$ phases are present in the negative electrode from Cell A1. Several ZrO$_2$ particulates are also observed, but ZrO$_2$ is not electrochemically active and is commonly seen in Zr-containing AB$_2$ alloys [14,15,23–27]. Based on the micrographs and EDS results of the negative electrode from Cell B1, the Zr$_x$Ni$_y$ (mixture of Zr$_7$Ni$_{10}$/Zr$_9$Ni$_{11}$/ZrNi/TiNi) phase remains intact while the AB$_2$ phase breaks into smaller pieces. Since both alloys are multi-phase in nature (Table 1), the existence of secondary phases
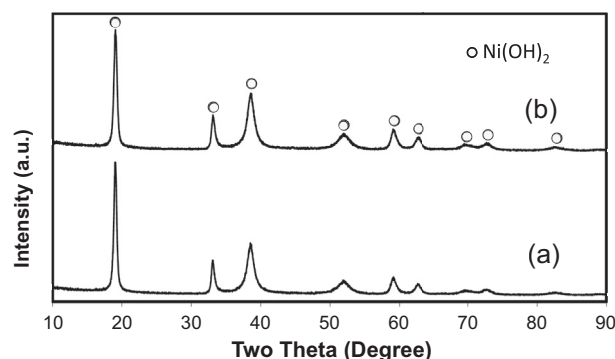

Fig. 4. XRD patterns of positive electrodes from Cells A1 (a) and B1 (b) at the end of C/2−C/2 cycling using Cu-K$_\alpha$ as the radiation source. Both patterns show materials are fully β-Ni(OH)$_2$.

Table 3
Concentrations of soluble contents in ppm in extracted solution after 24-h Soxhlet extraction.

	Parts	Zr	Ti	V	Al	Mn	Ni
Cell A2	Positive electrode	0.2	<0.04	2.5	6.3	0.04	<0.02
	Negative electrode	0.3	0.06	21.0	7.0	<0.03	<0.02
	Separator	0.1	<0.04	25.0	3.5	0.05	<0.02
Cell B2	Positive electrode	0.2	<0.04	<0.1	5.8	0.04	<0.02
	Negative electrode	0.3	0.06	<0.1	7.0	<0.03	<0.02
	Separator	0.1	<0.04	<0.1	2.7	0.04	0.2

Table 4
Compositions of spots identified in Fig. 5b and d determined by EDS.

	Ti	Zr	V	Cr	Mn	Fe	Co	Ni	Al	B/A	Phase
Fig. 5b-1	11.3	21.3	11.6	4.6	14.5	0.1	0.0	36.0	0.5	2.06	AB_2
Fig. 5b-2	11.7	21.4	10.5	4.0	13.8	0.0	0.0	38.1	0.6	2.02	AB_2
Fig. 5b-3	16.5	22.5	1.2	0.2	2.0	0.0	0.0	57.2	0.2	1.56	Zr_7Ni_{10}
Fig. 5b-4	1.5	91.4	1.0	0.3	1.3	0.0	0.0	4.5	0.0	0.08	ZrO_2
Fig. 5d-1	16.9	28.1	0.0	0.4	3.8	0.0	3.9	46.6	0.0	1.22	Zr_9Ni_{11}
Fig. 5d-2	12.8	32.0	0.0	0.1	1.9	0.0	2.5	50.4	0.0	1.23	Zr_9Ni_{11}
Fig. 5d-3	9.7	23.0	0.0	5.7	15.1	0.0	4.5	41.6	0.1	2.05	AB_2
Fig. 5d-4	8.7	26.7	0.0	6.5	18.0	0.3	5.7	33.9	0.1	1.82	AB_2
Fig. 5d-5	9.6	25.8	0.0	5.7	16.5	0.2	5.5	36.5	0.0	1.82	AB_2

cannot be the explanation for the difference in mechanical integrity. PCT hysteresis, a measurement of energy needed for the elastic deformation of the crystal lattice near the metal/hydride interface during hydriding [28–30], was demonstrated to be closely related to the pulverization rate during cycling [31–33]. Alloy B has a much larger PCT hysteresis and therefore is prone to more severe pulverization during cycling, which is observed in the SEM/EDS analysis.

XRD patterns before and after cycling for Alloys A and B are shown in Fig. 6. In both alloys, the C14/C15/Zr_xNi_y abundance ratios remain about the same, and minor traces of ZrO_2 and TiO_2 are observed after cycling. Where a passive $La(OH)_3$ layer forms on the surfaces of cycled AB_5 MH alloys as a result of oxidation [5], when AB_2 MH alloy corrodes in KOH solution, the majority of the oxidation products leaches out into the electrolyte and leaves behind a non-passive, porous oxide layer. Combining the SEM/EDS results with the XRD results suggests that the oxidation/passivation of the negative electrode is not a direct cause of capacity degradation for either alloy, but the continuous pulverization of the AB_2 phase during cycling can be linked to the capacity loss in cells with Alloy B. The only observation that can be linked to the capacity degradation in Alloy A is the high leaching rate of V seen in the Soxhlet

extraction analysis. It will be investigated further in the next section.

3.3. Discussion

In Fig. 2, while capacity degradation in Alloy B remains consistent throughout the entire cycle life and is related to the pulverization of the MH alloy, capacity degradation in Alloy A increases suddenly at around 75% of cycle life, and little evidence of pulverization is seen. DC resistances of the cells measured at every 50 cycles are plotted vs. the cycle number in Fig. 7 and shows that the DC resistances in Cells B1 and B2 increase at a constant rate. This constant increase in resistance in the cells with Alloy B can be associated with the pulverization in the negative electrode, in which newly formed surface area continuously wicks away electrolyte from the separator to fill the interfaces. By the same token, the sudden jump in DC resistance in Cells A1 and A2 is also related to the loss of electrolyte, but by a different mechanism: cell venting. The cells with Alloy A vent when the inner pressures reach 2.6 MPa, which buildup over time during cycling and push open the vent mechanism. Typically, the oxygen that evolves from the surface of
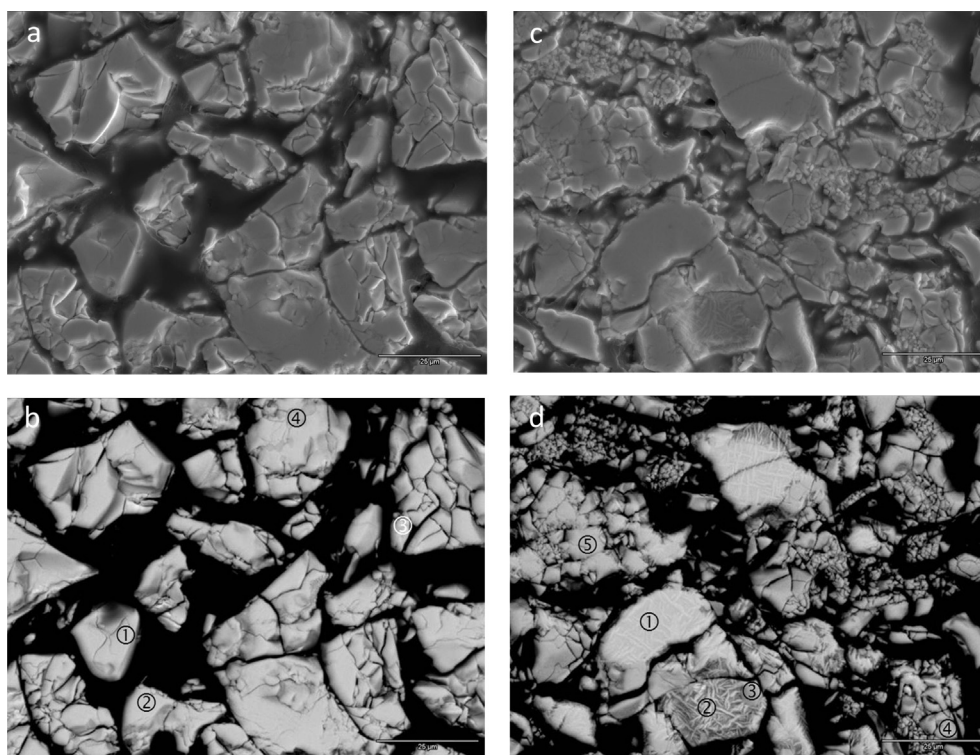

Fig. 5. SEM SEI (a) and BEI (b) micrographs of the negative electrode from Cell A1 and SEI (c) and BEI (d) micrographs of the negative electrode from Cell B1 after the conclusion of cycle life testing.
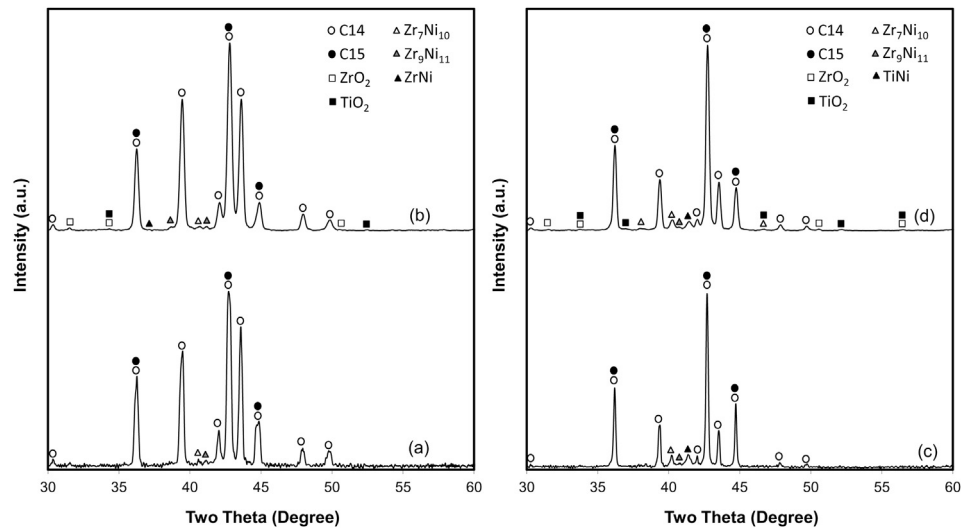
Fig. 6. XRD patterns of negative electrodes from Cell A1 before (a) and after cycling (b) and Cell B1 before (c) and after cycling (d) using Cu-K$_\alpha$ as the radiation source.

the positive electrode during overcharge recombines with the stored hydrogen in the negative electrode to prevent the buildup of pressure [34,35]. In this case, there are two possible explanations for the increase in inner pressure in Cells A1 and A2. The first possibility is that V leaches out from the negative electrode, arrives on the positive electrode surface, lowers the oxygen evolution potential (the opposite effect of Mg, Cd, and Ca, which raises the oxygen evolution potential [36]), generates more oxygen, and triggers more hydrogen evolution from the negative electrode. The second possible explanation is that the porous surface oxide on the negative electrode becomes thicker and less gas permeable due to the high leaching rate of V and impedes oxygen-hydrogen recombination, causing pressure buildup in the cell.

In order to test these two theories, a leaching experiment was performed that isolated the alloys. Alloy powder from both alloys was exposed to 30 wt.% KOH solution at 100 °C for 4 h. Concentrations of metallic elements in the solution were studied by ICP, and the results are summarized in Table 5. Alloy A (V-containing alloy) not only leaches out large amounts of V, but also more Zr, Ti, Al, and Cr than Alloy B (V-free alloy). Keeping in mind the short time scale and static nature of this experiment, this observation does not contradict the EDS analysis on the cycled positive electrodes that show more contamination in cells with Alloy B; the continuous pulverization of Alloy B exposes new alloy surfaces for oxide formation that contributes to more leaching of metallic elements into the electrolyte over time that then accumulate on the positive electrode. Any detrimental effect of contamination would result in pre-mature and incomplete charging, setting off the gas recombination reaction and $-\Delta V$ cut-off much earlier and resulting in lower capacity. This charging behavior was observed minimally in the cells, and further supports the conclusion that the contamination of the positive electrode is unlikely to be responsible for the capacity degradation in cells containing these two alloys.

The surfaces of the alloys after etching in 30 wt.% KOH solution at 100 °C for 4 h are compared in Fig. 8. While the surface of Alloy A is covered by oxide outgrowth (presumably TiO$_2$), the surface of Alloy B has fewer fine particulates. Along with the ICP leaching results, this indicates that Alloy A is more readily oxidized than Alloy B. Then given the high leaching rate of V in Alloy A, KOH penetrates the oxide layer pores to access more of the alloy, which in turn leaches out more V oxidation products, propagating the porous oxide layer deeper into the alloy particles over time. Once the oxide layer is thick enough to noticeably hinder diffusion to the

active surfaces, it impedes the oxygen-hydrogen recombination reaction and raises the inner pressure in the cell after enough cycling. XRD patterns (Fig. 6) indicate that the cycled samples of Alloys A and B contain the same amount of oxide, and with the
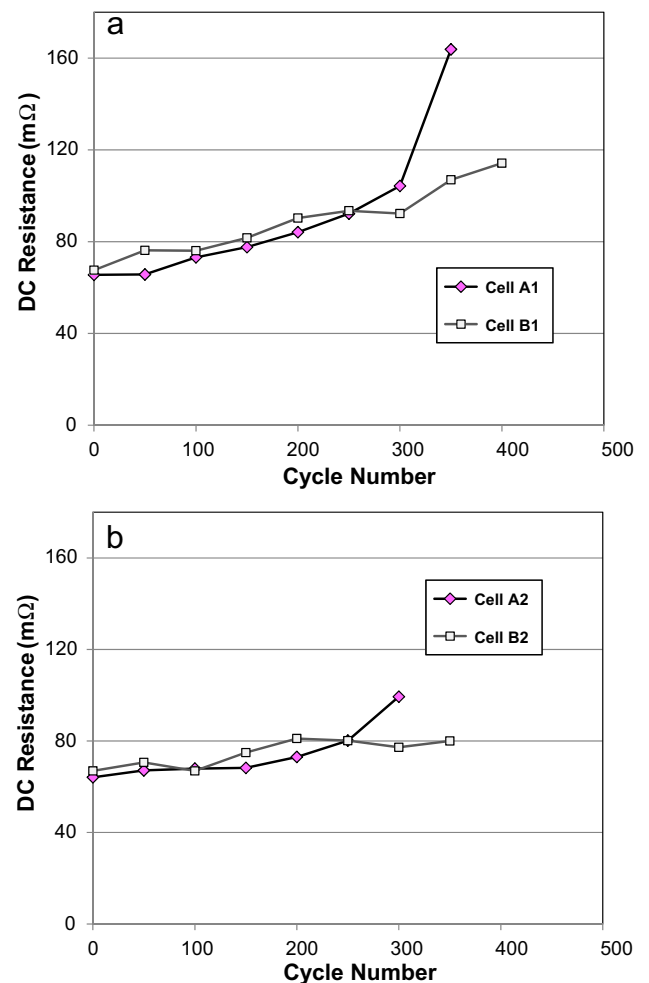

Fig. 7. Plots of DC resistance measured at the end of every 50 cycles for cells under C/2−C/2 (a) and 1C−1C (b) cycling conditions.

Table 5
Concentrations of soluble contents in ppm in solution after etching 1 g of alloy powder in 7 ml 30 wt.% KOH solution at 100 °C for 4 h.

	Zr	Ti	V	Al	Co	Cr
Alloy A	67.8	0.9	46.3	88.7	<0.06	0.8
Alloy B	56.7	0.4	<0.01	33.0	<0.06	<0.05

larger surface area for Alloy B, the surface oxide of Alloy A should be thicker than that of Alloy B. A thicker oxide layer for Alloy A also agrees with its larger M_S value. It can be concluded that the high leaching rate of V in Alloy A contributes to the formation of a thicker oxide layer on the negative electrode surface, initiating the failure mechanism that leads to shortened cycle life in Alloy A.

In contrast to the failure mode for Alloy A, the main failure mode for cells containing Alloy B is pulverization associated with hydride/dehydride cycling that manifests itself with high PCT hysteresis. Additional supporting evidence for this theory is the crystallite size obtained from whole pattern fitting and Rietveld refinement of XRD patterns from cycled electrodes. The crystallite size obtained from a heavily cycled Alloy B is 669 Å and is smaller than the size obtained from Alloy A under similar conditions (1252 Å). The smaller crystallite size of cycled Alloy B suggests incomplete discharge of the positive electrode in a negative limited configuration (smaller

Fig. 8. SEM SEI micrographs of the alloy surfaces of Alloy A (a) and Alloy B (b) after a 100 °C hot bath in 30 wt.% KOH for 4 h.

negative electrode capacity compared to positive electrode) at the end of cycle life. While the high PCT hysteresis and high pulverization found in Alloy B is related to the composition and structure of the alloy, they are not necessarily related to the lack of V leaching or even to the lower rates of oxidation. Hysteresis is a bulk property of the material while leaching and oxidation affects the surface. Many V-free alloys tend to exhibit similar hysteresis values and the associated pulverization behavior with cycling [14,15]. Influences to cycle life from elements other than V may exist as well. But the levels of their contributions are similar or small as seen from the ICP results from cycled electrodes in Table 3 and the leaching experiment in Table 5, and therefore, were not compared in this paper.

4. Summary

Two different failure mechanisms are attributed to the capacity degradation seen in a V-containing and a V-free Laves phase-based AB_2 metal hydride alloy. Both alloys form a porous oxide layer on the surface of the alloys, but the high leaching rate of V in the V-containing alloy allows a thicker oxide layer to form, which eventually impedes gas recombination in the cell and sets off a chain of events leading to venting and shortened cycle life. The cells with the V-containing alloy show less capacity degradation before venting occurs compared to the cells with the V-free alloy, but after venting, the degradation increases sharply and surpasses the V-free alloy. Cells containing the V-free alloy show linear capacity degradation throughout the cycle life due to the continuous pulverization of the main AB_2 phase. Understanding the failure modes will enable further alloy development work to improve the cycle life performance of AB_2 MH alloys.

References

[1] M.A. Fetcenko, S.R. Ovshinsky, K. Young, B. Reichman, C. Fierro, J. Koch, F. Martin, W. Mays, T. Ouchi, B. Sommers, A. Zallen, J. Alloys Compd. 330–332 (2002) 752.
[2] K. Young, M.A. Fetcenko, T. Ouchi, F. Li, J. Koch, J. Alloys Compd. 469 (2009) 406.
[3] S. Yasuoka, Y. Magari, T. Murata, T. Tanaka, J. Ishida, H. Nakamura, T. Nohma, M. Kihara, Y. Bada, H. Teraoka, J. Power Sources 156 (2006) 662.
[4] K. Young, J. Nei, Materials 6 (2013) 4574.
[5] X. Zhou, K. Young, J. West, J. Regalado, K. Cherisol, J. Alloys Compd. 580 (2013) S373.
[6] S.V. Mitrokhin, T.N. Bezuglaya, V.N. Verbetsky, J. Alloys Compd. 330–332 (2002) 146.
[7] S. Li, S. Ji, J. Sun, J. Dalian Maritime Univ. 29 (2003) 79.
[8] X. Yu, B. Xia, Z. Wu, N. Zu, Mater. Sci. Eng. A373 (2004) 303.
[9] J.C. Wang, R.H. Yu, Q. Liu, Mater. Sci. Technol 13 (2005) 166.
[10] K. Young, M.A. Fetcenko, F. Li, T. Ouchi, J. Koch, J. Alloys Compd. 468 (2009) 482.
[11] S.S. Makridis, A. Ioannidou, E. Zupanic, A. Prodan, E.S. Kikkinides, A.K. Stubos, Mater. Sci. Forum 636–637 (2010) 887.
[12] H.A. Peretti, A. Visintin, L.V. Mogni, H.L. Corso, J.A. Gamboa, D. Serafini, W.E. Triaca, J. Alloys Compd. 354 (2003) 181.
[13] B.H. Liu, Z.P. Li, S. Suda, J. Electrochem. Soc. 149 (2002) A537.
[14] K. Young, T. Ouchi, J. Koch, M.A. Fetcenko, J. Alloys Compd. 510 (2012) 97.
[15] K. Young, T. Ouchi, B. Huang, M.A. Fetcenko, J. Alloys Compd. 511 (2012) 242.
[16] J.M. Joubert, M. Latroche, A. Percheron-Guégan, J. Alloys Compd. 231 (1995) 494.
[17] K. Young, B. Huang, R.K. Regmi, G. Lawes, Y. Liu, J. Alloys Compd. 506 (2010) 831.
[18] F. Stucki, L. Schlapbach, J. Less-Comm. Met. 74 (1980) 143.
[19] B. Liu, X.Y. Wang, H.T. Yuan, Y.S. Zhang, D.Y. Song, Z.X. Zhou, J. Appl. Electrochem. 29 (1999) 855.
[20] B. Liu, H. Yuan, Y. Zhang, Int. J. Hydrogen Energy 29 (2004) 453.
[21] H. Bode, K. Dehmelt, J. Witte, Electrochim. Acta 11 (1966) 1079.
[22] M. Pourbaix, Atlas of Electrochemical Equilibria in Aqueous Solution, National Association of Corrosion Engineers, Houston, TX 77027, 1974, p. 241.
[23] K. Young, J. Nei, T. Ouchi, M.A. Fetcenko, J. Alloys Compd. 509 (2011) 2277.
[24] K. Young, T. Ouchi, J. Koch, M.A. Fetcenko, J. Alloys Compd. 477 (2009) 749.
[25] K. Young, T. Ouchi, B. Reichman, W. Mays, R. Regmi, G. Lawes, M.A. Fetcenko, A. Wu, J. Alloys Compd. 489 (2010) 202.
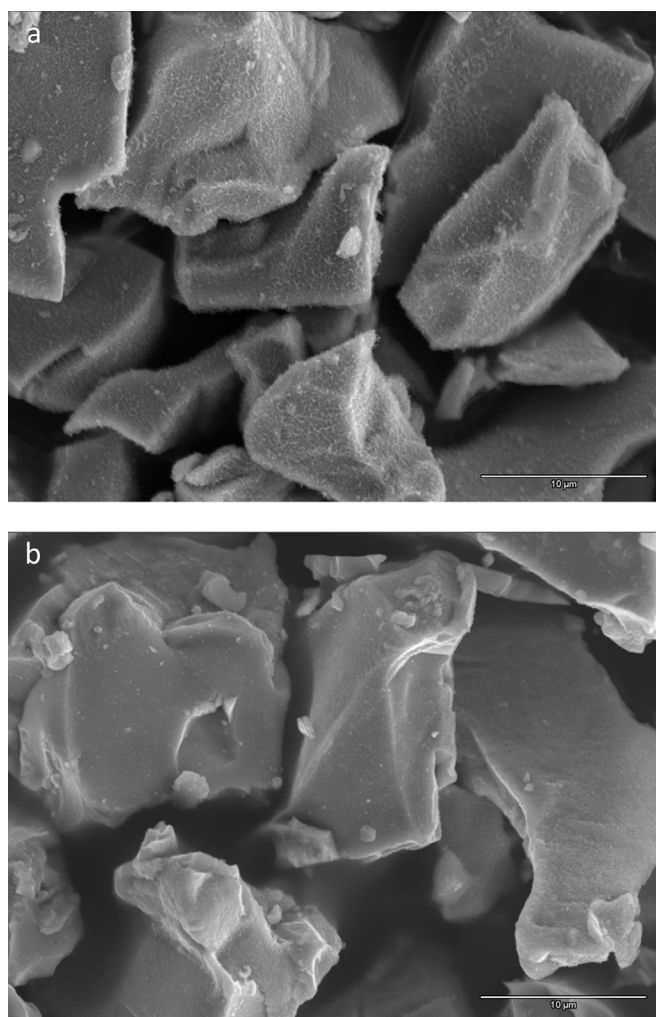
[26] L.A. Bendersky, K. Wang, I. Levin, D. Newbury, K. Young, B. Chao, et al., J. Power Sources 218 (2012) 474.
[27] K. Young, T. Ouchi, B. Huang, B. Reichman, R. Blankenship, J. Alloys Compd. 575 (2013) 65.
[28] N.A. Scholtus, W.K. Hall, J. Chem. Phys. 39 (1963) 868.
[29] B.J. Makenas, H.K. Birnbaum, Acta Metall. Mater. 28 (1980) 979.
[30] R. Balasubramaniam, Acta Metall. Mater. 41 (1993) 3341.
[31] K. Young, T. Ouchi, M.A. Fetcenko, J. Alloys Compd. 480 (2009) 428.

[32] K. Young, T. Ouchi, W. Mays, B. Reichman, M.A. Fetcenko, J. Alloys Compd. 480 (2009) 434.
[33] K. Young, T. Ouchi, M.A. Fetcenko, J. Alloys Compd. 480 (2009) 440.
[34] K. Young, A. Wu, Z. Qiu, J. Tan, W. Mays, Int. J. Hydrogen Energy 37 (2012) 9882.
[35] Z. Ye, D. Noréus, J. Power Sources 208 (2012) 232.
[36] C. Fierro, A. Zallen, J. Koch, M.A. Fetcenko, J. Electrochem. Soc. 153 (2006) A492.